

Research Article

Open Access



A hierarchical host microstructure enables regulated inner Li deposition for stable Li metal electrodes

Zhendong Li^{1,2} , George Z. Chen³ , Di Hu², Xiayin Yao^{1,4}, Zhe Peng^{1,4}

¹Ningbo Institute of Materials Technology and Engineering, Chinese Academy of Sciences, Ningbo 315201, Zhejiang, China.

²Department of Chemical and Environmental Engineering, Faculty of Science and Engineering, University of Nottingham Ningbo China, Ningbo 315100, Zhejiang, China.

³Department of Chemical and Environmental Engineering, Faculty of Engineering, University of Nottingham, Nottingham NG7 2RD, UK.

⁴Center of Materials Science and Optoelectronics Engineering, University of Chinese Academy of Sciences, Beijing 100049, China.

Correspondence to: Prof. Di Hu, Department of Chemical and Environmental Engineering, Faculty of Science and Engineering, University of Nottingham Ningbo China, 199 Taikang East Road, Yinzhou District, Ningbo 315100, Zhejiang, China. E-mail: di.hu@nottingham.edu.cn; Prof. Xiayin Yao, Ningbo Institute of Materials Technology and Engineering, Chinese Academy of Sciences, 1219 Zhongguan West Road, Zhenhai District, Ningbo 315201, Zhejiang, China. E-mail: yaoxy@nimte.ac.cn; Prof. Zhe Peng, Ningbo Institute of Materials Technology and Engineering, Chinese Academy of Sciences, 1219 Zhongguan West Road, Zhenhai District, Ningbo 315201, Zhejiang, China. E-mail: pengzhe@nimte.ac.cn

How to cite this article: Li Z, Chen GZ, Hu D, Yao X, Peng Z. A hierarchical host microstructure enables regulated inner Li deposition for stable Li metal electrodes. *Microstructures* 2024;4:2024059. <https://dx.doi.org/10.20517/microstructures.2024.13>

Received: 19 Feb 2024 **First Decision:** 11 Mar 2024 **Revised:** 3 Apr 2024 **Accepted:** 12 Apr 2024 **Published:** 15 Oct 2024

Academic Editor: Zaiping Guo **Copy Editor:** Fangyuan Liu **Production Editor:** Fangyuan Liu

Abstract

Dendritic lithium (Li) deposition is a critical issue hindering the development of next-generation high-energy-density Li metal batteries (LMBs). Confining Li deposition within a three-dimensional host is a general strategy to suppress the volume expansion of the Li electrode. However, precise control of continuous Li growth in the pore space of the host is rarely investigated, which is a crucial issue to enable a high utilization ratio of the hosted Li for practical LMBs. Herein, a novel hierarchical host structure possessing a multifunctional secondary porous structure to regulate the continuous Li growth with high uniformity and reversibility is proposed. The secondary porous structure consisting of carbon nanotubes, nickel and Li₂O-enriched solid electrolyte interphase is *in-situ* generated via lithiation reaction of a modified nickel foam scaffold, exhibiting high lithiophilicity, fast Li⁺ transportation and charge transfer. The LMB utilizing Li metal electrodes hosted by this rational structure achieved a stable cycling over 300 cycles with a practical LiFePO₄ positive electrode (~2.5 mAh cm⁻²) at 0.5C/0.5C in the voltage window of



© The Author(s) 2024. **Open Access** This article is licensed under a Creative Commons Attribution 4.0 International License (<https://creativecommons.org/licenses/by/4.0/>), which permits unrestricted use, sharing, adaptation, distribution and reproduction in any medium or format, for any purpose, even commercially, as long as you give appropriate credit to the original author(s) and the source, provide a link to the Creative Commons license, and indicate if changes were made.



2.5–4.4 V. This work provides a novel approach to designing the host microstructure for constructing more stable Li metal electrode in practical LMBs.

Keywords: Li metal battery, Li metal electrode, dendrite, volume expansion, carbon nanotube, host structure

INTRODUCTION

Developing high-energy-density rechargeable batteries is becoming a central topic in scientific and industrial communities due to the ever-growing market of electric vehicles^[1]. The state-of-the-art lithium (Li) ion batteries relying on graphite negative electrodes with a low specific capacity (372 mAh g^{-1}) are approaching their energy density limits, which are still below the required levels for application in long-range electric vehicles^[2]. Consequently, the exploration of alternative materials to replace graphite is urgently needed. Li metal is considered as a promising candidate due to its ultrahigh theoretical specific capacity ($3,860 \text{ mAh g}^{-1}$) and the lowest redox potential (-3.04 V vs. the standard hydrogen electrode)^[3,4]. However, its utilization in rechargeable batteries is challenged by several issues. Unlike the Li intercalation/extraction reactions in graphite, which involve a low volume expansion of $\sim 8\%$ upon charge/discharge processes^[5], the Li stripping/plating processes occurring on the hostless Li surface can cause a large volume expansion over 100% for a negative/positive capacity ratio of 1. The latter is a critical factor for the practical configuration of Li metal batteries (LMBs)^[2]. Moreover, the electrodeposited Li often forms in dendritic or mossy morphologies, which not only aggravate the uneven volume expansion but also pierce the fragile solid electrolyte interphase (SEI). Additionally, the SEI cracks consume fresh Li for secondary side reactions with the electrolyte during cycling. These factors lead to rapid battery failure and eventual safety accidents^[4]. Hence, stabilizing Li metal electrodes for long-term cycling is a prerequisite for widespread application of LMBs.

Numerous research endeavors have been devoted to addressing the aforementioned issues associated with Li metal electrodes. Apart from optimizing electrolytes and constructing artificial protection layers to improve the stability of the Li/electrolyte interface^[6–13], three-dimensional host structures are deemed effective in mitigating the volume expansion of deposited Li due to the void space serving as a preserved Li storage place^[14,15]. Additionally, the large areal surface of the host, based on carbon- and metal-based scaffolds, can reduce the local current density and provide more nucleation sites for Li deposition^[16–18]. Besides these general advantages, further optimizations of the host structures were achieved through the surface structuring of the substrates (nano-fibers, nano-spheres, nano-flowers, *etc.*) to increase the surface area with decreased local current density^[19–21], and/or the application of lithiophilic surface coatings (SnO , CuO , ZnO , *etc.*) to guide Li deposition across the inner space of the host^[22–24]. Despite these advancements, an important issue has rarely been addressed yet, namely, the regulation of continuous Li growth in the pore space. This is particularly important for applying Li metal electrodes in practical batteries that use a low Li amount in the negative electrode and a thick positive electrode, thus requiring a high utilization ratio of Li metal in the host structure^[2]. In a conventional three-dimensional e^- conducting scaffold with void pores, after the initial nucleation and deposition of a thin Li layer, further Li growth will occur on the top of the host due to the fast e^- conduction to the host surface in an uncontrolled manner [Figure 1A], thereby limiting the Li-host composite electrode performance under high-capacity cycling conditions.

Recent studies show that hierarchical hosts consisting of a primary conducting backbone with large pores to accommodate Li electrodeposition with global structural stability, and a multifunctional secondary porous structure to regulate continuous Li growth with high uniformity within the host, can be a good approach to addressing the above issue^[25,26]. However, the complex synthesis processes of these hierarchical structures remain a concern. Herein, we propose a novel hierarchical host structure obtained through a facile casting-

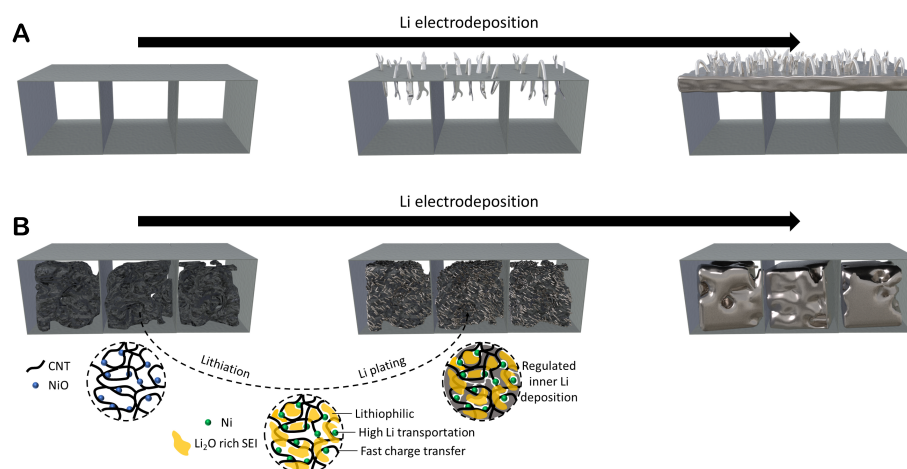


Figure 1. Schematic illustration of Li electrodeposition in (A) conventional host structure with void pores and (B) hierarchical host structure with multifunctional secondary porous structures.

annealing process. Specifically, nickel foam (NF), which has a higher Li affinity than that of Cu, is selected as the primary backbone^[16], which is filled with carbon nanotubes (CNT). Through a facile and scalable annealing process, abundant NiO particles are generated within the CNT network. This substructure is then decorated by metallic Ni particles and Li₂O-enriched SEIs after the initial lithiation, resulting in multifunctional secondary porous structures featuring high lithiophilicity, fast Li⁺ transportation and charge transfer [Figure 1B]. The LMB utilizing Li metal electrodes hosted by this rational structure achieved stable cycling over 300 cycles with a practical positive electrode loading ($\sim 2.5 \text{ mAh cm}^{-2}$). This remarkable performance highlights the critical importance of regulating continuous Li growth within the inner pores of the host structure to achieve high utilization of the hosted Li. The proposed design and the results from this work are promising to applying three-dimensional hosted Li electrodes in developing safer high-energy-density LMBs. As other metal electrodes (such as sodium, zinc, and potassium) also suffer from the large volume expansion and dendrite growth^[27–29], the host structure proposed in this work is expected to improve the cycling performances of these metal electrodes for a wide application range in the energy storage field.

MATERIALS AND METHODS

Materials

NF was purchased from Suzhou Sinero Tech. Co. Ltd. CNTs were obtained from Jiangsu XFNANO Materials Tech. Co. Ltd. Polyacrylonitrile (PAN) and N-Methyl-2-pyrrolidinone (NMP) were purchased from Aladdin. LiPF₆, ethylene carbonate (EC), diethyl carbonate (DEC), and fluoroethylene carbonate (FEC) were purchased from Suzhou Dodo Chem. All chemicals were used directly without further treatment.

Sample preparation

CNT-coated NF (denoted as NF-CNT) was prepared via a conventional casting process. CNT and PAN with a weight ratio of 2:8 were mixed by adding appropriate amount of NMP solvent (with a PAN:NMP weight ratio of 1:9), followed by stirring until a homogeneous mixture was obtained. Afterward, the slurry was cast on an 8 cm × 8 cm NF. The as-obtained NF-CNT was dried at 60 °C for 2 h, followed by heating in air at a rate of 5 °C min⁻¹ up to 500 °C, and then maintained for 30 min to obtain the NF-CNT500 sample. In our previous work, the carbon-like cross-linker derived from the pyrolysis of the PAN binder can greatly stabilize the cycling performance of silicon electrodes that also feature large volume expansion^[30]. Thus, PAN was selected in this work not only as the binder material during casting procedure of CNT on NF but

can also be converted into a carbon-like cross-linker with good robustness at the Ni oxidation temperature of 500 °C. Moreover, the Ni oxidation temperature should not exceed 500 °C. Otherwise, an over-oxidized state of NF with a thick NiO layer can easily catch fire during the molten Li infusion process. The NF500 sample was obtained through the same annealing process using pure NF without CNTs. The composite electrodes (NF500@Li, NF-CNT500@Li) were obtained by soaking NF500 and NF-CNT500 in molten Li at 250 °C.

Characterizations

The surface morphology and elemental distribution were characterized using a scanning electron microscope (SEM, FEI, Quanta FEG250). The Raman spectra were performed using a Renishaw in Via Reflex Raman spectrometer. The crystalline phase was determined by X-ray diffraction (XRD, Bruker, D8 Advance Davinci) using a diffractometer with Cu K α ($\lambda = 1.5406$ Å) radiation. Surface chemistry analysis was carried out using X-ray photoelectron spectroscopy (XPS, Axis Ultra DLD) with a radiation source of Mg K α at 15 kV and 6.67 mA. Brunauer-Emmett-Teller (BET) measurements were performed using Micromeritics ASAP 2020.

Electrochemical characterization

For cell assembly, 2,032 coin cells were used, in which 70 μ L electrolyte of 1 M LiPF $_6$ in EC:DEC:FEC (1:1:1 by vol.) was introduced to a Celgard 2320 separator. For the Li|Ni half cells, NF, NF500 or NF-CNT500 was used as the working electrode, and a Li foil served as both the counter and reference electrode. For the Li|Cu half cells, a Cu foil functioned as working electrode, and Li, NF500@Li or NF-CNT500@Li was employed as both the counter and reference electrode. The half cells were cycled by Li plating on the working electrode at selected capacity and current density, followed by Li stripping up to a cut-off voltage of 1 V at the same current density. For the symmetrical cells, Li, NF500@Li or NF-CNT500@Li was placed at each side of the separator, and the symmetrical cells were cycled under galvanostatic condition with fixed current density and capacity of 1 mA cm $^{-2}$ -1 mAh cm $^{-2}$. For the full cells, Li, NF500@Li or NF-CNT500@Li was used as the negative electrode, which was paired with a LiFePO $_4$ positive electrode with an areal capacity of ~ 2.5 mAh cm $^{-2}$ (area: 1.54 cm 2 , specific loading: ~ 16 mg cm $^{-2}$). Each full cell was pre-cycled at charge/discharge rates of 0.1C/0.1C for five cycles, followed by long-term cycling at 0.5C/0.5C in the voltage window of 2.5-4.4 V. All the batteries were assembled in an argon-filled glove box. All the battery tests were performed using LAND CT2001A battery testers at 30 °C.

The electrochemical impedance spectroscopy (EIS) and cyclic voltammetry (CV) measurements were carried out using a potentiostat/galvanostat 1470E from Solartron. The impedance spectra were recorded in a frequency range of 10 6 to 10 $^{-1}$ Hz with a voltage perturbation of 10 mV. The CV curves were performed at various scanning rates ranging from 4 to 12 mV s $^{-1}$ in the range of ± 15 mV.

RESULTS AND DISCUSSION

Figure 2A-D shows the photo of the investigated samples. Compared to the gray appearance of NF [Figure 2A], the black color of NF-CNT indicates the successive incorporation of CNTs in the porous structure of NF [Figure 2B]. The latter was verified by the characteristic D ($\sim 1,331$ cm $^{-1}$) and G ($\sim 1,567$ cm $^{-1}$) bands on the Raman spectrum of NF-CNT [Supplementary Figure 1]. Further oxidation of NF-CNT via the annealing treatment resulted in a slight color change of the electrode [Figure 2C], arising from the formation of NiO particles in the host structure according to the Raman spectrum of NF-CNT500 [Supplementary Figure 1]^[31]. Besides, the D/G peak ratios of NF-CNT and NF-CNT500 were 0.97 and 1.30, respectively. This change should be due to the formation of a carbon-like cross-linker derived from the pyrolysis of PAN on CNTs. The incorporated secondary porous structure consisting of CNTs and NiO in

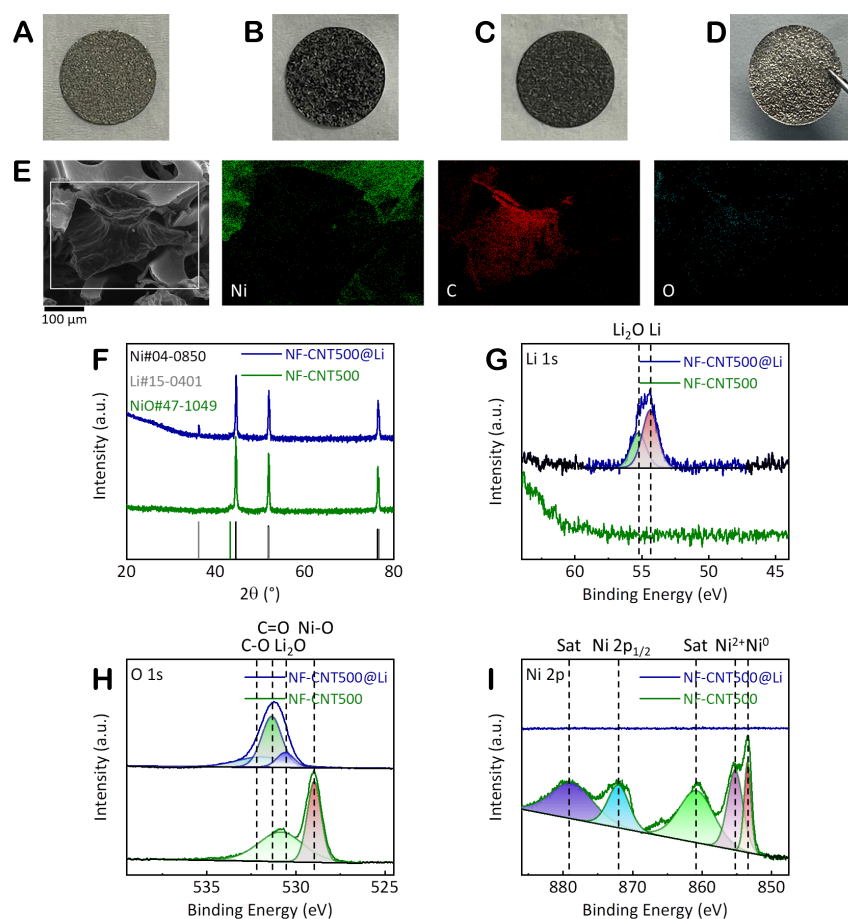


Figure 2. Photo of (A) NF, (B) NF-CNT, (C) NF-CNT500 and (D) NF-CNT500@Li. (E) SEM and EDS images of NF-CNT500. (F) XRD spectrum of NF-CNT500 and NF-CNT500@Li. (G) Li 1s, (H) O 1s and (I) Ni 2p XPS spectra of NF-CNT500 and NF-CNT500@Li.

NF-CNT500 was also demonstrated by SEM and energy dispersive spectroscopy (EDS) images [Figure 2E and Supplementary Figure 2], where distinct Ni, C and O distributions were observed clearly. Consistently, the successive incorporation of the secondary porous structure was also demonstrated by BET measurements, where a BET surface area of $4.57 \text{ m}^2 \text{ g}^{-1}$ was obtained for NF-CNT500, while it was not detectable for NF since only large void pores exist in this host [Supplementary Figure 3].

The presence of NiO endows NF-CNT500 with a high lithiophilicity, as shown by the high-quality NF-CNT500@Li composite electrode obtained via molten Li infusion into NF-CNT500 [Figure 2D]. As shown in Supplementary Figure 4, progressive Li propagation was clearly observed upon molten Li infusion process in NF-CNT500, demonstrating its great lithiophilicity. Furthermore, by weighting the electrode before/after molten Li diffusion, the mass loading of Li on NF-CNT500 is about 10 mg cm^{-2} in the case of excessive molten Li. It should be noted that the mass loading of Li in NF-CNT500 can be controlled by limiting the amount of molten Li. Consistently, an additional peak related to metallic Li ($\sim 36.2^\circ$) was clearly observed on the XRD pattern of NF-CNT500@Li compared to that of NF-CNT500 [Figure 2F]. The surface chemistry of NF-CNT500 and NF-CNT500@Li was further analyzed by XPS. As shown in Figure 2G, a peak comprising Li and Li_2O components was observed on the Li 1s spectrum of NF-CNT500@Li, where the minor signal of Li_2O besides the major peak of Li should arise from the slightly oxidized Li surface of the composite electrode during the sample transfer into the XPS chamber. This is also the case for the surface

chemistry revealed by the O 1s spectrum of NF-CNT500@Li [Figure 2H]. It should be noted that no Ni signal was observed on the Ni 2p spectrum of NF-CNT500@Li [Figure 2I], indicating the great lithiophilicity of NF-CNT500 to adsorb a high quantity of Li in the host so that the surface components on the skeletons were fully covered beneath. Owing to the lithiation reaction of NiO ($\text{NiO} + 2\text{Li} \rightarrow \text{Ni} + \text{Li}_2\text{O}$) during initial conversion of NF-CNT500, Ni and Li_2O should exist on the initially cycled NF-CNT500 surface. Thus, XPS study on the initially cycled NF and NF-CNT500 without molten Li infusion was also performed. As shown in Supplementary Figure 5A, compared with the Ni 2p spectrum of the cycled NF electrode showing the metallic Ni peaks, the similar peaks observed for the cycled NF-CNT500 electrode demonstrated the reduction of NiO into metallic Ni on the surface. Meanwhile, ROCO_2Li and Li_2O signals were observed on the O 1s spectra of the investigated samples [Supplementary Figure 5B]. It is noteworthy that both ROCO_2Li and Li_2O can arise from the reductive decompositions of the carbonate-based electrolyte^[9]; however, the stronger intensity of Li_2O peak on the O 1s spectrum of NF-CNT500 compared with that of NF indicates the supplementary contribution from the lithiation of NiO. Since these species arise from the initial lithiation reaction of NiO on the surface of the electrode, they should be incorporated as SEI components on NF-CNT500.

The electrochemical behaviors of Li plating on the investigated hosts were studied using Li||Ni half cells. As shown in Figure 3A, the hosts decorated by Ni oxides (NF500 and NF-CNT500) exhibited sharply different potential profiles during initial Li electroplating compared with that of NF, where the potential dips during the early stage of plating were much milder for NF500 and NF-CNT500, reflecting a more uniform nucleation process on the skeletons of these hosts. The related nucleation overpotential (difference between the potential dip and plateau) and deposition overpotential (potential plateau) are shown in Figure 3B, where the nucleation overpotentials are ~240.9, ~88.1, and ~70.1 mV for NF, NF500, and NF-CNT500, respectively, demonstrating the effect of the lithiophilic Li_2O -enriched interphase to reduce the energy barrier of Li nucleation. It is noteworthy that the oxide layer can generate an impeding interface for the charge transfer despite its lithiophilicity, as shown by the high deposition overpotential of ~93.9 mV on NF500 compared to ~56.7 mV on NF. However, this drawback can be efficiently compensated by the conducting CNT network in the secondary porous structure of NF-CNT500, leading to a reduced deposition overpotential of ~37.5 mV. As a consequence, the rational secondary porous structure enabled a sharply improved cycling coulombic efficiency (CE) of Li plating/stripping at 1 mA cm^{-2} - 1 mAh cm^{-2} [Figure 3C], where the average CE on NF-CNT500 was 96.2%, compared with 90.3% and 88.7% on NF and NF500, respectively.

The high interfacial stability on NF-CNT500 was also demonstrated by EIS study on the Li||Ni half cells. Before cycling, the interfacial impedance (semi-circle on EIS spectrum) of the cell using NF-CNT500 was much lower than those using NF and NF500 [Supplementary Figure 6]. It should be noted that no SEI layer was formed at this state of NF-CNT500, and the much lower interfacial impedance reflects the high charge transfer dynamism on the native surface of NF-CNT500. The EIS spectra of Li||Ni half cells using NF, NF500 and NF-CNT500 after 10, 25 and 50 cycles at 1 mA cm^{-2} - 1 mAh cm^{-2} were separately recorded [Supplementary Figure 7A-C]. Using the equivalent circuit diagram shown in Supplementary Figure 8A, the ohmic impedance related to the ionic conductivity of electrolyte (R_{ohm}), the SEI impedance related to Li^+ migration (R_{SEI}), and charge transfer impedance related to the e^- and Li^+ transfers involved in electrochemical reactions (R_{ct}) were separated revealed. As shown in Supplementary Figure 8B, the difference in R_{ohm} was not obvious due to the sufficient electrolyte amount introduced to the half cells. However, sharply reduced R_{SEI} [Supplementary Figure 8C] and R_{ct} [Supplementary Figure 8D] were observed for NF-CNT500, indicating a stable SEI layer with great Li^+ conducting ability on NF-CNT500.

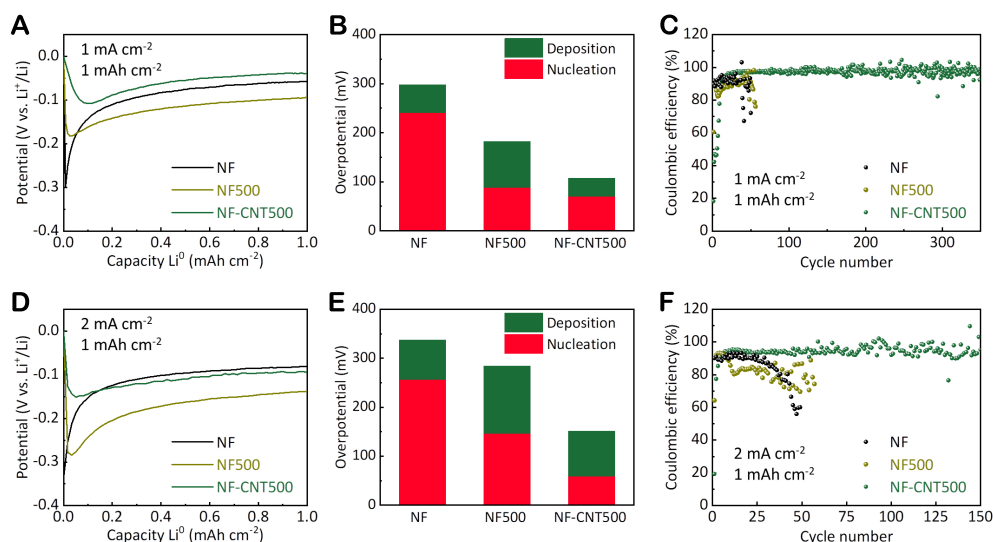


Figure 3. (A) Potential profile of initial Li electroplating with related (B) nucleation/deposition overpotentials and (C) cycling CE of Li plating/stripping on the investigated hosts at 1 mA cm⁻²-1 mAh cm⁻². (D) Potential profile of initial Li electroplating with related (E) nucleation/deposition overpotentials and (F) cycling CE of Li plating/stripping on the investigated hosts at 2 mA cm⁻²-1 mAh cm⁻².

Thanks to the multifunctional secondary porous structure in NF-CNT500, good electrochemical performance of Li electrodes was retained at an elevated current density of 2 mA cm⁻². As shown in Figure 3D and E, the Li nucleation overpotential was further increased to ~256.4 mV on NF, and a high value of ~146.3 mV was also achieved on NF500 despite its lithiophilicity, indicating the existence of a rate-determining step prior to the nucleation process that needs a fast Li⁺ transportation to avoid a supplementary energy dissipation rooted in the transfer kinetic. The latter was well addressed by NF-CNT500 due to the great Li conducting ability of the secondary porous structure, resulting in a low nucleation overpotential of ~58.9 mV. As well, the best cycling CE of Li electrodes at 2 mA cm⁻²-1 mAh cm⁻² also belonged to NF-CNT500 [Figure 3F] with an average CE of 94.8%, compared with 84.3% and 81.8% on NF and NF500, respectively, demonstrating the ability of NF-CNT500 to withstand stable Li plating/stripping at high current density. By further raising the current density and capacity up to 5 mA cm⁻²-5 mAh cm⁻², which match the actual requirement for constructing practical LMBs, the cell using NF-CNT500 still exhibited the best cycling stability [Supplementary Figure 9]. Furthermore, a CNT-attached Ni foil annealed at 500 °C (denoted as Ni foil-CNT500) has been fabricated and compared with that of NF-CNT500 in terms of Li protective ability. As shown in Supplementary Figure 10, the Li||Ni half cell using NF-CNT500 showed much better cycling stability than using Ni foil-CNT500, demonstrating the importance of the hierarchical host microstructure for Li metal protection. Besides the Li||Ni half cells revealing the ability of NF-CNT500 to promote a stable Li plating/stripping process, Li||Cu half cells were also tested to assess the cycling stability of the pre-lithiated NF-CNT500@Li composite electrode. As shown in Supplementary Figure 11, the best cycling performance was achieved on NF-CNT500@Li, where the average CEs are 91.1%, 88.6% and 96.3% for the cells using Li, NF500@Li and NF-CNT500@Li, respectively.

To reveal the role of the secondary porous structure in regulating the inner Li deposition, the Li deposition morphologies were studied by means of SEM and EDS. As shown in Figure 4A and B, at a Li plating capacity of 1 mAh cm⁻², dendritic Li deposits were loosely distributed on the skeletons of NF without any ordered manners. However, for NF-CNT500, sharply different Li plating behavior was observed. As shown in Figure 4C and D, the deposited Li was tailored into small and compact granules that were evenly distributed in the entire host space. The EDS images further illustrate the inability of the bare NF scaffold to

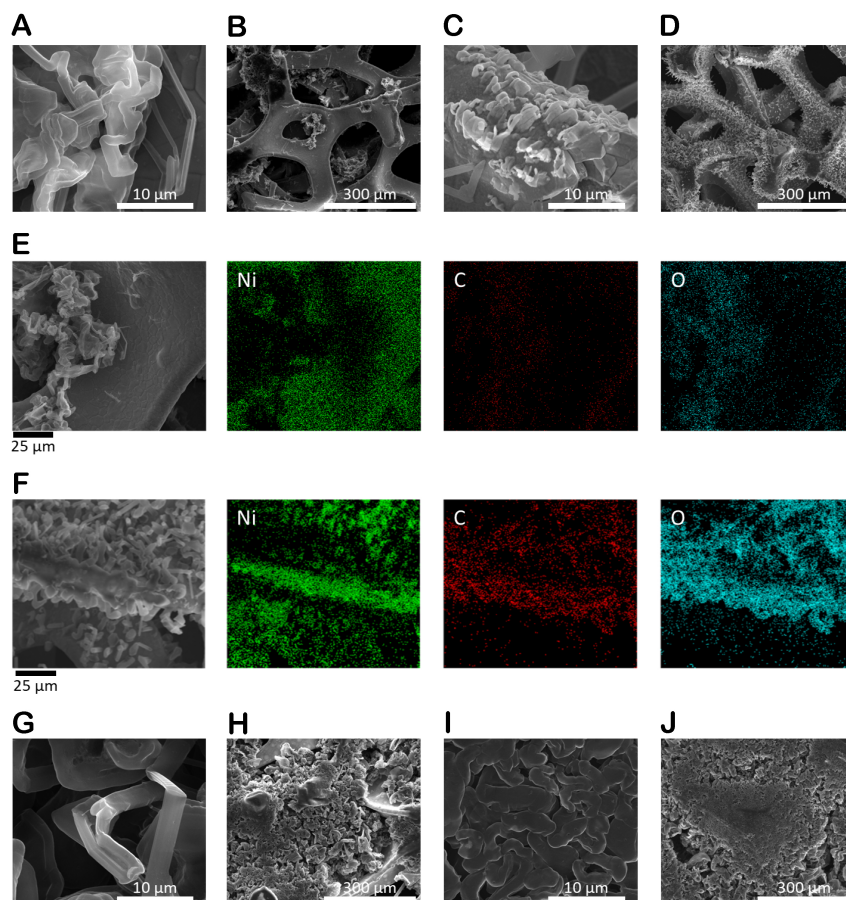


Figure 4. SEM images of (A and B) NF and (C and D) NF-CNT500 at a Li plating capacity of 1 mAh cm^{-2} . SEM and EDS images of (E) NF and (F) NF-CNT500 at a Li plating capacity of 1 mAh cm^{-2} . SEM images of (G and H) NF and (I and J) NF-CNT500 at a Li plating capacity of 4 mAh cm^{-2} .

regulate the inner Li deposition [Figure 4E], which should be a general concern for other pure metal hosts. Although the C and O signals can arise from the SEI layer derived from electrolyte decomposition, the overlapped Ni, C and O elements still give insights into the guided Li deposition by the CNT-based secondary porous structure [Figure 4F]. Similar features were also observed on the cross-section SEM and EDS images. As shown in Supplementary Figure 12A, Li deposits were mainly gathered on the top of NF due to the lack of medium to guide the inner Li deposition. In contrast, uniform Li deposition was guided inside the host structure of NF-CNT500 [Supplementary Figure 12B]. Dendritic filaments were also observed in the amplified zones of the cross-section images of NF [Supplementary Figure 12C and D], while granular Li deposits were evenly distributed on the skeletons of NF-CNT500 [Supplementary Figure 12E and F], demonstrating its ability to guide inner Li deposition in the host structure with high uniformity. As the Li plating capacity increased to a practical value of 4 mAh cm^{-2} , the pores of NF were fully filled with dendritic Li deposits [Figure 4G and H], clearly illustrating the problem shown in Figure 1A. Meanwhile, a heterogeneous distribution of Li deposits was also observed in the internal pores of NF [Supplementary Figure 13A]. In contrast, uniform and compact Li deposits were observed in both the top and inner pores of NF-CNT500 [Figure 4I and J, Supplementary Figure 13B], demonstrating the rationality of the hierarchical structure of NF-CNT500, in which the Ni skeletons provide large pores for preserved Li storing space and act as a mechanical scaffold to suppress volume

expansion, and the secondary porous structure featured with high lithiophilicity, fast Li^+ transportation and charge transfer enables guided Li deposition in the host with high uniformity and reversibility.

After demonstrating the advantage of the hierarchical structure of NF-CNT500, the NF-CNT500@Li composite electrode was fabricated via molten Li infusion [Figure 2D] and used in LMBs to assess its suitability as a substitute for a bare Li electrode. The symmetrical cells were first assembled to study the transfer kinetic and stability at the electrode/electrolyte interface. By performing CV scanning within a voltage window of ± 15 mV at different scanning rates, the averaged transfer kinetic was then estimated. For the cells using bare Li [Supplementary Figure 14A] and NF500@Li [Supplementary Figure 14B], the CV curves displayed minimal dependence on the scanning rate, while hysteresis feature towards the two voltage boundaries was observed for the cell using NF-CNT500@Li [Supplementary Figure 14C], signifying the existence of a capacitive redox process probably related to the Li adsorption/desorption and/or Li insertion/extraction through the CNT network. By converting the CV curves into Tafel plots, two quasi-symmetrical peaks vs. 0 V were observed for the cells using bare Li [Figure 5A] and NF500@Li [Figure 5B], corresponding to the interfacial polarization caused by the sluggish transfer kinetics. In contrast, the cell using NF-CNT500@Li exhibited a unique peak well centering at 0 V, reflecting an extremely low polarization enabled by fast transfer kinetic at the electrode/electrolyte interface [Figure 5C]. Consistently, the exchange current density revealed from the Tafel plot of the cell using NF-CNT500@Li is 2.137 mA cm^{-2} [Supplementary Figure 15], which is of magnitudes higher than those of Li ($0.00141 \text{ mA cm}^{-2}$) and NF500@Li ($0.00624 \text{ mA cm}^{-2}$).

The Li protection ability was further examined by the long-term cycling of the symmetrical cells. As shown in Figure 5D, at 1 mA cm^{-2} - 1 mAh cm^{-2} , the cells using bare Li achieved a drastic polarization increase in less than 15 h because of the fast accumulation of thick side products on the electrode surface. The cell using NF500@Li extended the lifespan over 200 h, followed by a drastic increase in polarization. The cell using NF-CNT500@Li realized a stable cycling over 500 h without obvious polarization increase, and more importantly, exhibited the lowest polarization from the beginning of the cycling, proving the simultaneously improved transfer kinetics and interfacial stability. Consistently, during the rate ability test of the symmetrical cells using Li, NF500@Li and NF-CNT500@Li, the cell using NF-CNT500@Li clearly showed a more stable voltage profile with a lower polarization compared with those using Li and NF500@Li [Supplementary Figure 16], indicating the fast Li^+ transportation and charge transfer ability.

Finally, the practical application of NF-CNT500@Li in full LMBs was assessed using a thick LiFePO_4 positive electrode ($\sim 2.5 \text{ mAh cm}^{-2}$). As shown in Figure 6A, the $\text{Li}|\text{LiFePO}_4$ cell showed a fast capacity fading in less than 75 cycles, while the fluctuating voltage profiles indicate a serious internal short-circuit caused by the uncontrolled Li deposition. The NF500@Li $|\text{LiFePO}_4$ cell cycled over 160 cycles followed by fluctuant CEs, probably due to the slow transfer kinetics hindering the full utilization of the active materials [Figure 6B]. Notably, stable cycling over 300 cycles with a capacity retention of 86.7% was achieved by the NF-CNT500@Li $|\text{LiFePO}_4$ cell [Figure 6C and D]. Considering the well-known high stability of the LiFePO_4 electrodes, the significantly improved performance of the NF-CNT500@Li $|\text{LiFePO}_4$ cell compared with that using bare Li or NF500@Li should arise from the superior NF-CNT500@Li electrode. These results demonstrate the good applicability of the proposed hierarchical structure for hosting stable Li metal electrodes in practical LMBs.

CONCLUSIONS

In this work, a multifunctional secondary porous structure was introduced to the conventional metal scaffold to enable regulated inner Li deposition for better cycling stability of the hosted Li electrode.

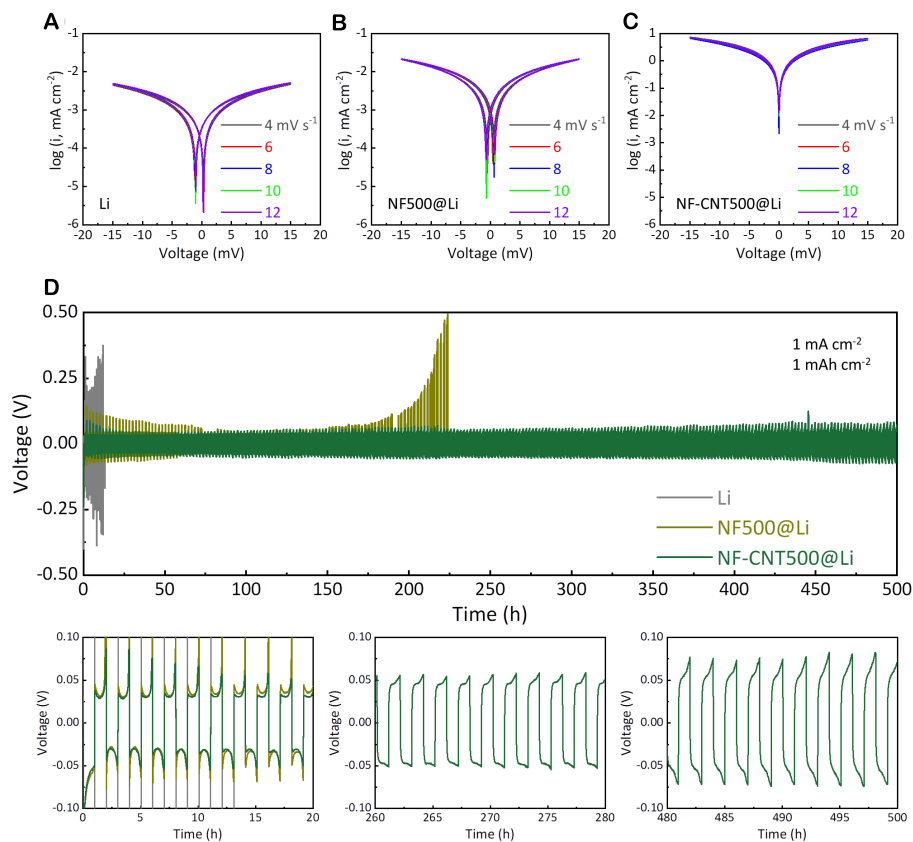


Figure 5. Tafel plot of symmetrical cells using (A) Li, (B) NF500@Li and (C) NF-CNT500@Li electrodes. (D) Voltage profile of symmetrical cells during long-term cycling.

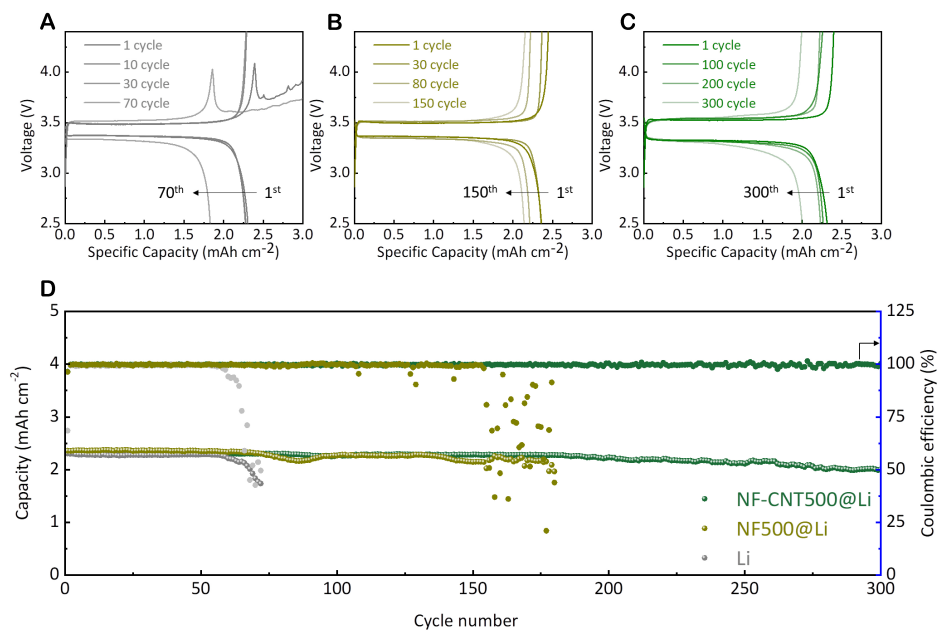


Figure 6. Charge-discharge profiles of LMBs using (A) Li, (B) NF500@Li and (C) NF-CNT500@Li electrodes. (D) Cycling performance of LMBs during long-term cycling. The cycling was carried out at charge/discharge rates of 0.5C/0.5C.

Specifically, the secondary porous structure consisting of CNTs, Ni and Li₂O-enriched SEI was incorporated in the Ni scaffold and endowed with high lithiophilicity, fast Li⁺ transportation and charge transfer. In addition to the mechanical confinement of the deposited Li by the Ni scaffold, the multifunctional secondary porous structure exhibited great ability to accelerate the Li⁺ transportation, reduce the Li nucleation barrier and boost the electrochemical reaction kinetic inside the host, resulting in highly compact and uniform Li deposition in the internal pores of the host, which cannot be achieved by the conventional metal hosts with void pores. Consequently, the investigated hierarchical host enabled stable Li plating/stripping with high CEs under different cycling conditions. Notably, the LMB using the composite Li electrode based on the hierarchical host stably cycled over 300 cycles with a practical positive electrode capacity ($\sim 2.5 \text{ mAh cm}^{-2}$), validating the rationality of the proposed host structure. This work emphasized the profound impact of the hierarchical structuration of the host on enhancing the cycling stability of Li metal electrodes. It is also expected to employ this strategy to improve the performance of other metal electrodes, showing a grand interest in developing next-generation secondary batteries.

DECLARATIONS

Authors' contributions

The conception and design of the work: Li Z, Peng Z

The acquisition and analysis of data: Li Z

The interpretation of data: Li Z, Hu D, Yao X, Peng Z

The writing and revising: Li Z, Chen GZ, Hu D, Yao X, Peng Z

The supervision: Chen GZ, Hu D, Yao X, Peng Z

Availability of data and materials

The raw data were listed in the [Supplementary Materials](#). Further data used to support the findings of this study are available from the corresponding author upon reasonable request.

Financial support and sponsorship

This work was supported by the National Natural Science Foundation of China (Grant No. 52250610214 and U21A2075), the Ningbo S&T Innovation 2025 Major Special Program (Grant No. 2021Z122), the Zhejiang Provincial Key R&D Program of China (Grant No. 2022C01072), the Jiangsu Provincial S&T Innovation Special Program for carbon peak and carbon neutrality (Grant No. BE2022007), and the Youth Innovation Promotion Association CAS (Y2021080).

Conflicts of interest

All authors declared that there are no conflicts of interest.

Ethical approval and consent to participate

Not applicable.

Consent for publication

Not applicable.

Copyright

© The Author(s) 2024.

REFERENCES

1. Xiao J, Shi F, Glossmann T, Burnett C, Liu Z. From laboratory innovations to materials manufacturing for lithium-based batteries. *Nat Energy* 2023;8:329-39. [DOI](#)
2. Liu J, Bao Z, Cui Y, et al. Pathways for practical high-energy long-cycling lithium metal batteries. *Nat Energy* 2019;4:180-6. [DOI](#)
3. Guo Y, Li H, Zhai T. Reviving lithium-metal anodes for next-generation high-energy batteries. *Adv Mater* 2017;29:1700007. [DOI](#)

4. Cheng XB, Zhang R, Zhao CZ, Zhang Q. Toward safe lithium metal anode in rechargeable batteries: a review. *Chem Rev* 2017;117:10403-73. DOI PubMed
5. Genieser R, Ferrari S, Loveridge M, et al. Lithium ion batteries (NMC/graphite) cycling at 80 °C: different electrolytes and related degradation mechanism. *J Power Sources* 2018;373:172-83. DOI
6. Lu Z, Li W, Long Y, et al. Constructing a high-strength solid electrolyte layer by in vivo alloying with aluminum for an ultrahigh-rate lithium metal anode. *Adv Funct Mater* 2020;30:1907343. DOI
7. Xu R, Shen X, Ma X, et al. Identifying the critical anion-cation coordination to regulate the electric double layer for an efficient lithium-metal anode interface. *Angew Chem* 2021;133:4261-6. DOI
8. Wang X, Li S, Zhang W, et al. Dual-salt-additive electrolyte enables high-voltage lithium metal full batteries capable of fast-charging ability. *Nano Energy* 2021;89:106353. DOI
9. He Y, Zhang Y, Wang Z, et al. In situ surface film formed by solid-state anodic oxidation for stable lithium metal anodes. *Adv Funct Mater* 2021;31:2101737. DOI
10. Ju Z, Jin C, Cai X, et al. Cationic interfacial layer toward a LiF-enriched interphase for stable Li metal batteries. *ACS Energy Lett* 2023;8:486-93. DOI
11. Liu Y, Tao X, Wang Y, et al. Self-assembled monolayers direct a LiF-rich interphase toward long-life lithium metal batteries. *Science* 2022;375:739-45. DOI
12. Shadike Z, Tan S, Lin R, Cao X, Hu E, Yang XQ. Engineering and characterization of interphases for lithium metal anodes. *Chem Sci* 2022;13:1547-68. DOI PubMed PMC
13. Wang Z, Du Z, Liu Y, et al. Metal-organic frameworks and their derivatives for optimizing lithium metal anodes. *eScience* 2024;4:100189. DOI
14. Li Z, Liang W, Chen J, et al. In-depth Li⁺ transportation in three-dimensionalized nanodiamond network for improved liquid and solid lithium metal batteries. *Nano Energy* 2023;110:108370. DOI
15. Liu L, Yin YX, Li JY, Wang SH, Guo YG, Wan LJ. Uniform lithium nucleation/growth induced by lightweight nitrogen-doped graphitic carbon foams for high-performance lithium metal anodes. *Adv Mater* 2018;30:1706216. DOI PubMed
16. Lu L, Zhang Y, Pan Z, Yao H, Zhou F, Yu S. Lithiophilic Cu-Ni core-shell nanowire network as a stable host for improving lithium anode performance. *Energy Stor Mater* 2017;9:31-8. DOI
17. Chi S, Liu Y, Song W, Fan L, Zhang Q. Prestoring lithium into stable 3D nickel foam host as dendrite-free lithium metal anode. *Adv Funct Mater* 2017;27:1700348. DOI
18. Liu B, Zhang Y, Wang Z, et al. Coupling a sponge metal fibers skeleton with in situ surface engineering to achieve advanced electrodes for flexible lithium-sulfur batteries. *Adv Mater* 2020;32:e2003657. DOI
19. Ye H, Xin S, Yin YX, Li JY, Guo YG, Wan LJ. Stable Li plating/stripping electrochemistry realized by a hybrid Li reservoir in spherical carbon granules with 3D conducting skeletons. *J Am Chem Soc* 2017;139:5916-22. DOI PubMed
20. Li S, Ma Y, Wei B. A lightweight, adhesive, dual-functionalized over-coating interphase toward ultra-stable high-current density lithium metal anodes. *Energy Environ Mater* 2021;4:103-10. DOI
21. Gong H, Chen Y, Chen S, et al. Fast-charging of hybrid lithium-ion/lithium-metal anodes by nanostructured hard carbon host. *ACS Energy Lett* 2022;7:4417-26. DOI
22. Tan L, Feng S, Li X, et al. Oxygen-induced lithiophilicity of tin-based framework toward highly stable lithium metal anode. *Chem Eng J* 2020;394:124848. DOI
23. Tan L, Li X, Cheng M, et al. In-situ tailored 3D Li₂O@Cu nanowires array enabling stable lithium metal anode with ultra-high coulombic efficiency. *J Power Sources* 2020;463:228178. DOI
24. Wu K, Zhao B, Yang C, Wang Q, Liu W, Zhou H. ZnCo₂O₄/ZnO induced lithium deposition in multi-scaled carbon/nickel frameworks for dendrite-free lithium metal anode. *J Energy Chem* 2020;43:16-23. DOI
25. Xue P, Liu S, Shi X, et al. A hierarchical silver-nanowire-graphene host enabling ultrahigh rates and superior long-term cycling of lithium-metal composite anodes. *Adv Mater* 2018;30:e1804165. DOI
26. He Y, Song L, Li Z, Yao X, Peng Z. Hosting Li⁰ in an activated lithiophilic polymer matrix with electrodeposition regulating spaces for stable lithium metal anodes. *Nano Energy* 2023;118:109027. DOI
27. Wang C, Zheng Y, Chen Z, et al. Robust anode-free sodium metal batteries enabled by artificial sodium formate interface. *Adv Energy Mater* 2023;13:2204125. DOI
28. Li G, Zhao Z, Zhang S, et al. A biocompatible electrolyte enables highly reversible Zn anode for zinc ion battery. *Nat Commun* 2023;14:6526. DOI PubMed PMC
29. Feng Y, Rao A, Zhou J, Lu B. Selective potassium deposition enables dendrite-resistant anodes for ultrastable potassium-metal batteries. *Adv Mater* 2023;35:2300886. DOI PubMed
30. Zhang Z, Jiang Y, Peng Z, et al. Facile pyrolyzed N-doped binder network for stable Si anodes. *ACS Appl Mater Interfaces* 2017;9:32775-81. DOI
31. Alastuey P, Pais Ospina D, Comedi D, Tirado M, Marin-ramirez O. On the properties of NiO powders obtained by different wet chemical methods and calcination. *J Am Ceram Soc* 2024;107:92-106. DOI